Parasternal Versus Apical View in Cardiac Natural Mechanical Wave Speed Measurements

Lana B. H. Keijzer, *Student Member, IEEE*, Mihai Strachinaru, Daniel J. Bowen,
Annette Caenen, *Member, IEEE*, Antonius F. W. van der Steen, *Fellow, IEEE*,
Martin D. Verweij, *Member, IEEE*, Nico de Jong, *Associate Member, IEEE*,
Johan G. Bosch, *Member, IEEE*, and Hendrik J. Vos, *Member, IEEE*

Abstract—Shear wave speed measurements can potentially be used to noninvasively measure myocardial stiffness to assess the myocardial function. Several studies showed the feasibility of tracking natural mechanical waves induced by aortic valve closure in the interventricular septum, but different echocardiographic views have been used. This article systematically studied the wave propagation speeds measured in a parasternal long-axis and in an apical four-chamber view in ten healthy volunteers. The apical and parasternal views are predominantly sensitive to longitudinal or transversal tissue motion, respectively, and could, therefore, theoretically measure the speed of different wave modes. We found higher propagation speeds in apical than in the parasternal view (median of 5.1 m/s versus 3.8 m/s, $p < 0.01$, $n = 9$). The results in the different views were not correlated ($r = 0.26$, $p = 0.49$) and an unexpectedly large variability among healthy volunteers was found in apical view compared with the parasternal view (3.5–8.7 versus 3.2–4.3 m/s, respectively). Complementary finite element simulations of Lamb waves in an elastic plate showed that different propagation speeds can be measured for different particle motion components when different wave modes are induced simultaneously. The *in vivo* results cannot be fully explained with the theory of Lamb wave modes. Nonetheless, the results suggest that the parasternal long-axis view is a more suitable candidate for clinical diagnosis due to the lower variability in wave speeds.

Index Terms—Aortic valve closure (AVC), lamb waves, myocardial stiffness, shear wave (SW) elastography, ultrasonic imaging.

Lana B. H. Keijzer, Mihai Strachinaru, Daniel J. Bowen, Annette Caenen, and Johan G. Bosch are with the Department of Cardiology, University Medical Center Rotterdam, Erasmus MC, 3000 CA Rotterdam, The Netherlands (e-mail: l.b.h.keijzer@erasmusmc.nl).

Antonius F. W. van der Steen, Martin D. Verweij, Nico de Jong, and Hendrik J. Vos are with the Department of Cardiology, University Medical Center Rotterdam, Erasmus MC, 3000 CA Rotterdam, The Netherlands, and also with the Department of Imaging Physics, Delft University of Technology, 2628 CN Delft, The Netherlands.

I. INTRODUCTION

HEART failure affects around 1–2% of all adults in developed countries and its prevalence is even more than 10% for people aged above 70 years [1]. The clinical course of heart failure is generally regarded as a consequence of structural and/or functional cardiac changes. Currently, the assessment of myocardial function primarily relies on the echocardiographic measurement of cardiac volumes, flow, and tissue velocity [1]–[3]. However, these measurements suffer from load-dependence issues and provide a rather indirect way of evaluating the myocardial function. The myocardial function could potentially be assessed more directly by evaluating cardiac stiffness [4], [5], a measure of the intrinsic cellular composition and structure of the heart muscle. At present, no noninvasive clinical routine method exists for measuring myocardial stiffness.

A highly promising tool for assessing myocardial stiffness noninvasively is ultrasound-based shear wave speed (WS) measurement [6]–[9], in which the WS is presumably linked to the myocardial elastic properties. Shear waves (SWs) in the cardiac wall can be induced externally using a vibration device [10]–[12] or an acoustic radiation force (ARF) [9], [13]–[18], or can occur naturally after aortic valve closure (AVC), mitral valve closure (MVC) [6]–[8], [19]–[22], and atrial contraction [23]–[25]. The propagation of these SWs over the myocardium can be measured using high frame rate (HFR) tissue Doppler imaging (TDI) or clutter filter wave imaging (CFWI) [26]. This study focuses on naturally induced SWs, which have the advantages of easier implementation in current clinical echocardiographic systems [27] and higher signal-to-noise ratios compared with externally induced SWs (TDI amplitudes of $\sim$40 mm/s [21] for natural SWs versus $\sim$10 mm/s [14] for external SWs). More specifically, we will focus only on SWs excited after AVC in the interventricular septum (IVS), as we previously found higher feasibility and lower intervolunteer variability for these SWs compared with those after MVC among healthy volunteers in parasternal long-axis view [28].

TABLE I
OVERVIEW OF DIFFERENT HUMAN STUDIES USING THE NATURAL SWS INDUCED AFTER AVC. THE FOLLOWING ABBREVIATIONS ARE USED IN THE TABLE: HV: HEALTHY VOLUNTEER(S); CA: CARDIAC AMYLOIDOSIS PATIENT; WS: WAVE SPEED; AVC: AORTIC VALVE CLOSURE; HCM: HYPERTROPHIC CARDIOMYOPATHY; TDI: TISSUE DOPPLER IMAGING; AND CFWI: CLUTTER FILTER WAVE IMAGING

Study	Subject	WS after AVC
Parasternal View		
Kanai, (2005) [19]	HV (n=1)	1 - 7 m/s (10-90 Hz)
Santos et al., (2019) [6]	HV (n=30)	3.5 ± 0.6 m/s (2.2 - 4.5 m/s)
Petrescu et al., (2019) [7]	HV (n=46)	3.75 ± 0.76 m/s
	CA (n=17)	5.63 ± 1.13 m/s
Strachinaru et al., (2019) [8]	HV (n=20)	3.61 ± 0.46 m/s (3.10 - 4.66 m/s)
	HCM (n=20)	5.13 ± 0.68 m/s (3.75 - 6.94 m/s)
Keijzer et al., (2019)* [28]	HV (n = 10)	Zonare 3.8 ± 0.4 m/s (3.23 - 4.25 m/s)
		Philips 3.2 ± 0.9 m/s (1.82 - 4.76 m/s)
This study	*HV (n=10)*	*3.7 ± 0.4 m/s (3.2 - 4.3 m/s)*
Apical View		
Brekke et al., (2014) [20]	HV (n=10)	5.41 ± 1.28 m/s
Santos et al., (2017) [29]	3D, HV (n=3)	4.2 ± 1.0 m/s (3.0 - 5.4 m/s)
Salles et al., (2019) [26]	HV (n=1)	TDI 5.12 ± 0.61 m/s
		CFWI 5.37 ± 0.44 m/s
This study	*HV (n=10)*	*5.7 ± 1.8 m/s (3.5 - 8.7 m/s)*

*The same volunteers have been used as in the current study. Some measurements have been repeated in order to have a complete data set with apical and parasternal view recordings in all sessions for all volunteers.

Even though the feasibility of natural SW detection using TDI in humans has been demonstrated, no consensus has been achieved regarding the preferred echocardiographic view for natural SW measurements. A parasternal view was reported by some studies [6]–[8], [19], whereas others used an apical view [20], [26], [29]. These different views depict a different component of particle motion in TDI, since TDI is most sensitive to axial particle motion (motion along the ultrasound beam). In a parasternal long-axis view, the IVS is oriented quasi-horizontally, resulting in a measurement of particle motion perpendicular to the IVS (transversal component). In an apical four-chamber view, the IVS is oriented vertically and, therefore, mainly, the particle motion parallel to the IVS is tracked (longitudinal component). An overview of previously reported WS in both echocardiographic views together with relevant specifications of each study is given in Table I. Table I shows that WS after AVC in healthy volunteers were generally higher in apical than in parasternal view. Furthermore, in general, a larger intervolunteer variability of WS between healthy volunteers was found in apical view studies. The observed differences in WS between parasternal and apical view might be due to the different orientations of the particle motion measured in both views, but it can also have other causes, such as intervolunteer

variability [6], [28], and the use of different echocardiographic systems [28] and data analysis methods [30]. Moreover, different sonographers might select slightly different windows in a standard echocardiographic view, inducing extra variabilities. Although, this article focuses on AVC, the effect of different views considered in this study could also be relevant for the SWs after MVC and the longitudinal wave-pattern after atrial contraction, since these different types of natural SWs have similar spatial and temporal characteristics.

The induced wave mode determines the main component of particle motion and should, thus, be taken into account when selecting a sonographic view for WS measurements. As the name implies, shear WS measurements were originally developed for assessing WS of bulk SWs dominated by transversal particle motion. Our earlier studies of natural waves in the heart, therefore, assumed the measurement of SWs dominated by transversal particle motion, ratifying the use of a parasternal view [21], [27]. Furthermore, Kanai [19] measured in 2005 a similar WS when tracking the transversal particle motion after AVC in the parasternal view and the longitudinal particle motion after AVC in apical view. Consequently, a coupling between the two directions of particle motion was assumed, representing one type of wave mode. However, the recent studies on natural SWs in both echocardiographic views report different WS for both views (see Table I). Therefore, we hypothesized that transversal, as well as longitudinal, wave modes are induced by AVC simultaneously and that a transversal mode is mainly measured in the parasternal view, while a longitudinal mode is measured in apical view. To test this hypothesis, a systematic study of SWs after AVC in apical and parasternal view is needed to minimize measurement uncertainties. To the best of our knowledge, such a study has not been performed yet.

The aim of the article presented here is, thus, to study the propagation speed of the SWs induced by AVC measured in a parasternal long-axis view and an apical four-chamber view in ten healthy volunteers. To improve our understanding of what we are measuring in both echocardiographic views, we performed complementary finite element simulations of Lamb wave propagation in the IVS—approached as an elastic plate immersed in liquid—while applying different forces and, therefore, inducing different wave modes. Based on the WS measurements on volunteers and simulation results, we will elaborate on possible theoretical explanations of the wave phenomena measured and discuss practical considerations. The outcomes of this study are expected to be important for determining the preferred view for robust and clinically meaningful natural WS measurements.

II. MATERIALS AND METHODS

A. Guided Waves in the Heart Wall

Elastic waves propagating in a medium that is bound in one or two directions such as the IVS, successively reflect at these boundaries, causing conversion between longitudinal waves and SWs. For a given frequency, only specific patterns of longitudinal waves and SWs can propagate. These patterns are called guided wave modes. Each propagating mode has a

specific, frequency-dependent WS, which makes these modes dispersive even in inviscid media (contrary to bulk waves). The IVS has a thickness (6–10 mm) smaller than the wavelength of natural SWs (~70 mm [28]), and guided waves are expected [31]–[36].

Guided waves propagating in a plate structure can be described by symmetric (S) Lamb wave modes, antisymmetric (A) Lamb wave modes and shear horizontal (SH) modes. Depending on the type of source, frequency, medium thickness, and material properties, various wave modes might be induced [31]. We will not consider SH modes, as the particle motion of these modes is along the plate surface perpendicular to the propagation direction [31] and is, therefore, probably hard to detect in cardiac parasternal and apical views. The A- and S-mode guided waves are characterized by different dispersion curves, as described in [31], [32], and [36]. S-modes are regularly referred to as longitudinal, and A-modes as transversal SWs because of the dominant particle motion with respect to the propagation direction in the centerline of the medium. Nevertheless, S-modes also include transversal particle motion and A-modes include longitudinal particle motion [36]. The ratio of the particle motion components of a specific mode is affected by the frequency of the SW and the thickness of the medium, especially near the boundaries of the medium. We focus on the zero-order S_0- and A_0-modes, since high order modes have not been detected yet in soft tissue plates [31].

Multiple studies on cardiac SW elastography used a theoretical Lamb wave model not only to improve the accuracy of tissue characterization methods, but also to extract additional information about certain material properties such as viscoelasticity. In 2005, Kanai [19] was the first to use an A_0-Lamb wave model to convert propagation speeds of SWs after AVC in humans into elastic and viscoelastic properties of the myocardium [19]. However, Vos *et al.* [21] only measured mild dispersion for SWs after AVC and MVC in pigs and, therefore, found a poor match with A_0-Lamb wave modes. This same model was used in studies using external sources like an external shaker [10], [11], [34], [35], and ARF [33], [37]. However, it should be noted that when using an ARF source in a parasternal long-axis view, the load is directed perpendicular to the myocardium, inducing, therefore, mainly the transversal particle motion (and thus the A_0-mode). On the contrary, for SWs induced by AVC, a more complex particle motion pattern is probably induced at the valvular plane as a consequence of the complex interaction between the valve leaflets, the abruptly decelerating blood flow, and the aortic valve annulus. Therefore, the nature of the wave modes that are induced in natural SW measurements is unknown. Note that the Lamb wave model is inherently associated with various limitations, as it assumes a homogeneous isotropic (visco) elastic plate submerged in fluid, while the myocardium has a complex geometrical shape, irregular blood-tissue interfaces, and other complex material properties such as muscular anisotropy. For example, several studies have shown that fiber orientation affects WS measurements using ARF [38]–[41]. However, the natural SWs have a lower frequency content than externally induced SWs and, therefore,
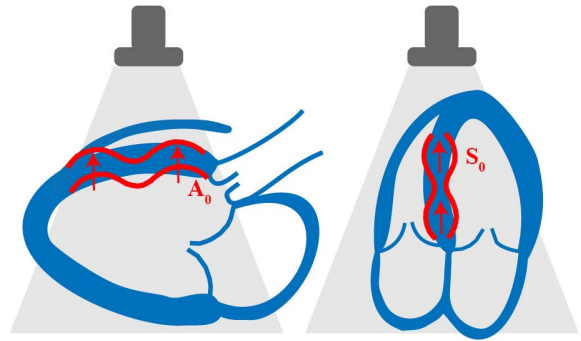

Fig. 1. In the parasternal long-axis view, mainly transversal particle motion is measured (left), while in the apical four-chamber view mainly longitudinal particle motion is measured (right) because of the angle dependence of TDI. It could be expected that if an A_0-mode and an S_0-mode are induced by the AVC, the A_0-mode dominated by transversal motion is mainly measured in the parasternal view, while the S_0-mode is mainly measured in apical view.

the effect of fiber orientation on natural SWs might be different than that on ARF-induced SWs [41].

As described before, mainly, the longitudinal particle motion is measured in the apical view, while transversal particle motion is measured in the parasternal view. Therefore, if both the A_0- and S_0-Lamb wave modes are induced by AVC, it is expected that the A_0-mode is mainly measured in the parasternal view and the S_0-mode in apical view, as schematically shown in Fig. 1. Nonetheless, to the best of our knowledge, the S_0-Lamb wave mode has not been used in other studies to describe the SWs induced by AVC measured in the apical view.

"Shear wave elastography" has become a generally accepted term for studies measuring wave propagation speeds that are presumably linked to the elasticity of the tissue. However, it should be noted that since we expect guided waves, the term "shear wave" might not be appropriate from a physics viewpoint to describe all phenomena observed in this study. Therefore, we will use from this point in the manuscript, the general terms "(mechanical) wave" and "wave propagation speed" (WS) to refer to related wave phenomena.

B. Finite Element Simulations of Guided Waves

Since different wave modes will, in general, have different WS along an individual path, we performed simulations to investigate what WS can be measured when different wave modes coexist. We studied differences in transversal and longitudinal particle motion and their propagation, as well as the influence of the excitation.

1) Model Setup: The 2-D simulations of a homogeneous plate immersed in water were performed in PZFlex (Thornton Tomasetti, Inc., Cupertino, CA, USA), a software package using the explicit finite-element method (FEM), to mimic guided wave propagation in plane strain conditions. The plate (10 mm × 187 mm) was modeled as an elastic material, with a bulk modulus of 22 MPa, a shear modulus of 16 kPa, and a density of 1050 kg/m^3. A shear modulus of 16 kPa corresponds to a shear WS of 4 m/s in an elastic bulk material, which is in the reported range of WS after AVC (see Table I).
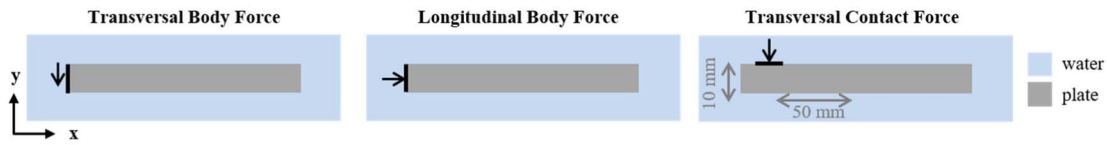
Fig. 2. Finite-element simulations; overview of different excitations used in PZFlex to simulate the wave propagation of guided waves in a plate structure submerged in water.
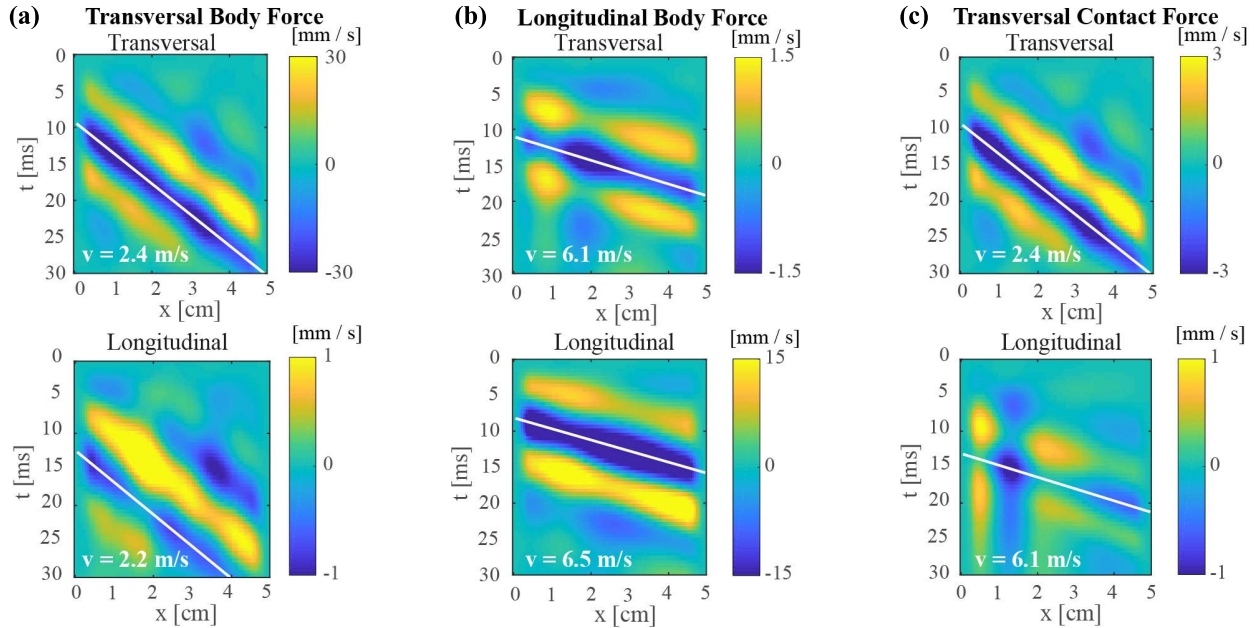

Fig. 3. Finite-element simulations; M-panels of transversal (top row) and longitudinal (bottom row) particle motion for a frequency band from 15 to 100 Hz obtained in a finite element simulation for different excitations on a plate submerged in water. An overview of different excitations is given in Fig. 2.

To avoid reflections at the end of the plate, the length was longer than the maximum length of the IVS ($\sim$100 mm in humans) and the distance that a bulk SW has traveled within a simulation time of 30 ms. Water surrounded the plate (total size of plate and water: 30 mm $\times$ 207 mm, absorbing boundary conditions) and was modeled with a bulk modulus of 22 MPa, zero shear modulus, and density of 1000 kg/m^3. To reduce the simulation times, the bulk moduli used in the simulation are smaller than the actual bulk moduli of tissue and water with a factor 100 [42]. This will only have a small effect on the Poisson ratio of the medium because the SW propagation speed c is still very small compared with the longitudinal propagation speed c_L ($c \ll c_L$) [42], [43]. Therefore, its effect on the dispersion curves is expected to be small. Quadrilateral elements were used and the element mesh size was chosen such that at least 48 elements fit in one wavelength at 160 Hz. Mechanical waves were induced by using three different excitations: 1) a transversal body force; 2) a longitudinal body force; and 3) a transversal contact force, as depicted in Fig. 2. For all excitations, a Blackman Harris driving function (pulse of three half-cycles) was used with a center frequency of 60 (-6 dB bandwidth: 30–95 Hz) or 160 Hz (-6 dB bandwidth: 80–252 Hz) in separate simulations. To validate the simulated phase speeds with theoretical dispersion curves within a 0–300 Hz frequency range, the results of the simulation with

the 160-Hz load was used to excite all frequencies within the selected range. The loading with the lower center frequency of 60 Hz resembled the frequency content of the natural waves in the IVS more realistically. Nonetheless, the aim of FEM simulations is not to mimic the *in vivo* situation as accurately as possible, but, as described before, to investigate different wave modes that coexist.

2) Data Analysis: The transversal and longitudinal particle motion, extracted along a horizontal line through the middle of the plate (50 mm length), was determined and assembled in two separate motion panels (M-panels), see the top and bottom row, respectively, in Fig. 3. These M-panels depict 1-D particle motion as a function of space and time. To avoid a bias in the WS estimation, the axial velocities in the M-panels were first resampled to have an equal number of pixels in space and time and were then mildly tapered along the edges of the M-panel in both directions. Moreover, a 15–100-Hz bandpass filter (sixth-order Butterworth) was applied to the axial tissue velocity data. Subsequently, a normalized Radon transform was used to determine the WS [21].

Phase speed values c_p were obtained by first applying a 2-D fast Fourier transform to the unfiltered M-panels, yielding the particle motion as a function of frequency and wavenumber, and then by selecting the wavenumber k with maximum intensity in the Fourier domain for each frequency f.
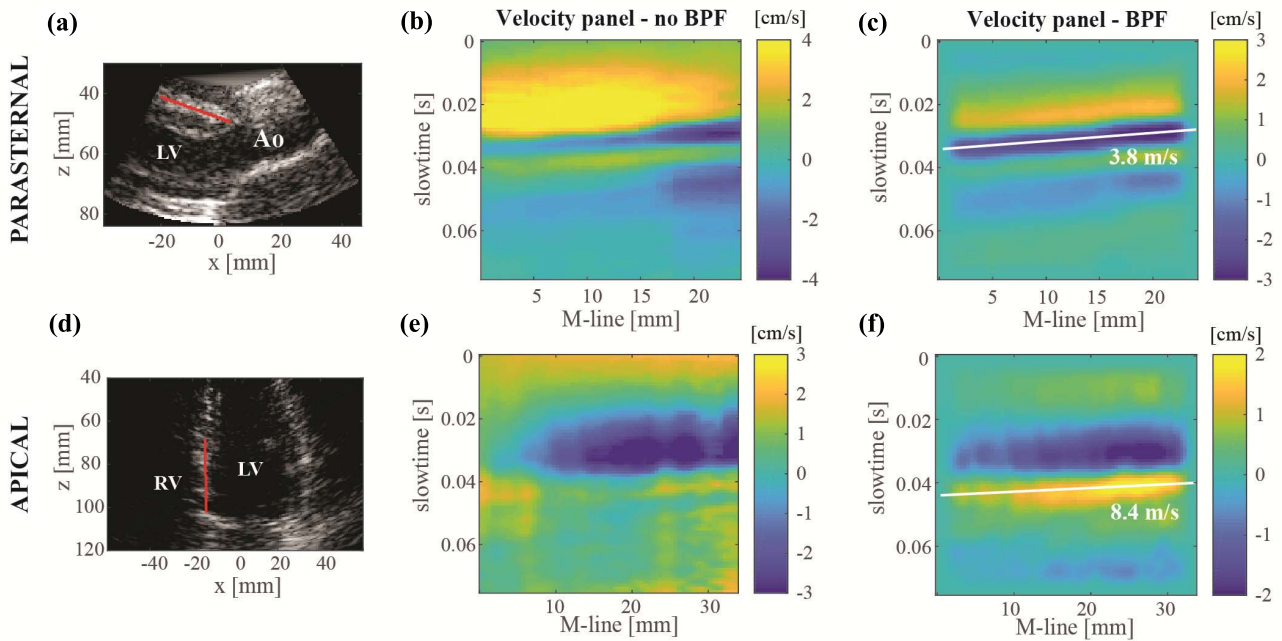
Fig. 4. Example of an M-line drawn in (a) parasternal and (d) apical view measurement and the (b) and (e) corresponding velocity panels. A bandpass filter from 15 to 100 Hz was applied in (c) and (f), and a Radon transform was used to determine the propagation speeds. Abbreviations: LV: left ventricle, Ao: aorta, RV: right ventricle, BPF: bandpass filter, and slow time: the time between frames.

Subsequently, the frequency-dependent phase speed was computed by dividing the frequencies with the corresponding wavenumber ($c_p = f/k$). No bandpass filter was applied to the M-panels before computing the phase speeds. The accuracy and correctness of the numerical phase speed plots were visually verified by comparing them to the theoretical dispersion curves of A_0-and S_0-modes in a nonstretched inviscid plate submerged in water as described in [32].

C. Natural Wave Elastography Measurements

WS measurements in ten healthy volunteers were performed to compare the WS in a parasternal long-axis view and in an apical four-chamber view. Details of the study population, data acquisition and analysis methods have been described previously [28] and are summarized below.

1) Study Population: Ten volunteers aged between 24 and 45 years were included (five males and five females). The study was approved by the local medical ethics committee (Erasmus MC MEC-2014-611) and all volunteers gave informed consent.

2) Data Acquisition: A clinical system programed by the manufacturer to enable an HFR imaging mode was used (Zonare ZS3, P4-1C probe, Mindray Innovation Center, San Jose, CA, USA). For each acquisition, an experienced sonographer first utilized a live B-mode with low frame rate (LFR) to position the probe in the correct echocardiographic view. Subsequently, HFR (1000 Hz) data were recorded after selecting the correct field-of-view (FOV) on the LFR images. The beamformed interquartile (IQ) data of a smaller FOV (approximately 5 cm × 7 cm, sector width of 55°) for 1.2 s in parasternal view and of the full FOV for 2 s in apical view was saved for offline processing.

During HFR recording, the live LFR B-mode was frozen. The HFR mode employed a diverging wave pulse-inversion transmission sequence for imaging, with 250 μs in between the two consecutive pulses of each frame. Gaussian-tapered sinusoidal pulses of seven cycles with a center frequency of 1.8 MHz were transmitted, with a mechanical index below 0.25. For every volunteer, five parasternal long-axis view HFR measurements were performed subsequently, while repositioning the probe in between the recordings. Also, one single HFR apical four-chamber view measurement (sector width of 84°) was performed within 30 min after the parasternal view measurements. Depending on the heart rate of the volunteers, one or two AVC events were measured within each recording. For every volunteer, all measurements were repeated after 21–182 days during a second scanning session. For volunteer 1–4, five instead of one apical view measurements were recorded in the second scanning session to test repeatability.

3) Data Analysis: Data analysis was performed in MATLAB R2017a (The Mathworks, Natick, MA, USA). A 250-Hz lowpass filter was applied to the IQ data in slow time (cut-off value of 5.2 cm/s, sixth-order Butterworth), to remove high-frequency TDI signal mainly arising from blood and noise. A one-lag autocorrelation technique was used to obtain axial tissue velocities [20]. Before computing the phase [20], the effect of speckle and noise was reduced with a spatial smoothing filter of 4 mm by 6.7°. The moment of AVC was determined based on the movements of the aortic and mitral valve and the overall motion of the heart in the derived TDI movies. In the frame at the moment of AVC, an anatomical M-line was manually drawn on the basal-mid ventricular part of the IVS, as shown in Fig. 4(a) and (d)

for parasternal and apical views, respectively. The location and length of these M-lines depended on the visibility of the wave propagation. The length of the M-lines drawn varied between 1.9 and 4.1 (parasternal view), and 2.5 and 5.8 cm (apical view). Since M-line location can affect the propagation speed measured [30] and since M-lines were drawn manually, variability was taken into account by drawing ten M-lines per acquisition. M-panels showing the axial tissue velocity of an M-line over time were used to visualize and quantify the wave propagation, see Fig. 4(b) and (e). As previously described for the FEM simulations, M-panels were first resampled and mildly tapered before applying a normalized Radon transform to determine the WS. A 15–100-Hz bandpass filter (sixth-order Butterworth) was applied to the axial tissue velocity data, since the waves after AVC were found to be in this frequency range [6]. For the parasternal view measurements, the minimum intensity corresponding to the particle motion away from the transducer was selected in the Radon domain. For the apical view measurements, the maximum intensity of the Radon transform was selected to determine WS [see Fig. 4(c) and (f)]. These extrema were most representative for the waves in the two views as shown in the unfiltered M-panels in Fig. 4(b) and (e).

D. Statistics

The statistical toolbox in MATLAB was used for the statistical analysis. The data were tested for being normally distributed by applying Kolmogorov–Smirnov tests. Since the data were not normally distributed, a nonparametric Wilcoxon signed-rank test was used to test whether measured differences are statistically different. A Bland–Altman analysis was performed to compare the WS for the two views by mean differences, limits of agreements (LOA) and range. Correlations were determined by computing linear correlation coefficients (Pearson) and by performing linear regressions. To compare our values with those in the literature, we computed the mean and standard deviation of the median values obtained per volunteer.

III. RESULTS

A. Simulation Results

Fig. 3 shows the simulation M-panels obtained for the transversal and longitudinal body force, and the transversal contact force, all with a center frequency of 160 Hz. Its resulting phase speed plots are visualized in Fig. 5 and correspond well with the theoretical dispersion curves of the A- and S-modes for an inviscid plate submerged in water as described by Li *et al.* [32]. For the transversal body force [Fig. 3(a)], phase speed plots of A_0 were found in the lower frequency range for both particle motion components, as can be expected from the predominantly transversal motion in such A_0-mode. For higher frequencies, a higher order A_1-mode was found to be dominant for longitudinal particle motion, whereas this was still the A_0-mode for transversal particle motion. The M-panels in Fig. 3 show similar WS for both transversal and longitudinal particle motion even though the magnitude of the transversal particle velocities was larger (ratio of 20.2 for
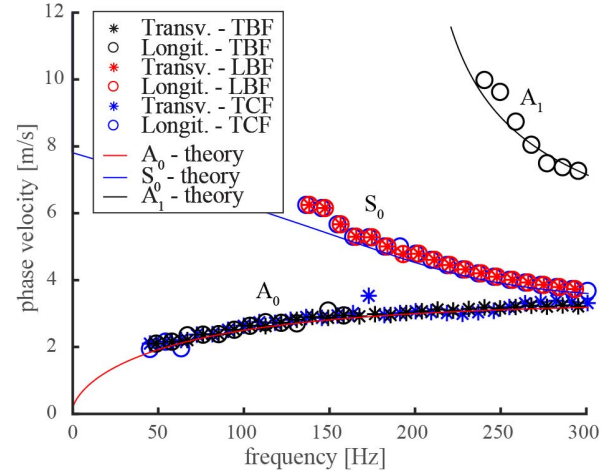

Fig. 5. Finite-element simulations; phase speed plots obtained for the transversal and longitudinal particle motion of the M-panels from Fig. 3. Different types of forces are used; a TBF, an LBF, and a TCF. Also, theoretical dispersion curves for a nonstretched inviscid plate submerged in water with a shear modulus of 16 kPa, a density of 1050 kg/m³ and a thickness of 10 mm [32] are depicted in the figure.

transversal versus longitudinal motion). This indicates that a single wave mode was present. For the longitudinal body force [Fig. 3(b)], phase speed plots of S_0 were found for both particle motion components, as can be expected from the predominantly longitudinal motion in such S_0-mode. Accordingly, similar WS were found for the M-panels in Fig. 3(b), indicating the presence of one wave mode. A longitudinal body force led indeed to larger particle velocities in the longitudinal direction (ratio of 0.07 for transversal versus longitudinal motion). For the simulations of the contact force [Fig. 3(c)], a phase speed plot similar to the theoretical A_0-mode was found for the transversal particle motion, while a phase speed plot similar to the theoretical dispersion curve of the S_0-mode was found for the longitudinal particle motion. Hence, different WS were obtained for the M-panels in Fig. 3(c) for the longitudinal and transversal particle motion. This suggests that different wave modes are simultaneously present. In this case, the transversal particle velocities were found to be larger, but in the same order as in the longitudinal direction (ratio of 3.7 for transversal versus longitudinal motion).

When using a center frequency of 60 Hz (data not shown), similar phase speed plots were obtained. However, for the contact force, the difference in transversal and longitudinal particle velocities was found to be larger (ratio of 11.7). This shows that depending on the source, different modes may be excited or the relative amplitudes of different modes may differ. Furthermore, the results show that when the particle motion in both directions is dominated by the A_0-mode for a frequency band of 15–100 Hz, the particle motion is largest in the transversal direction. The contrary holds for the S_0-mode. Translating these results to cardiac valve closure, they indicate that depending on the wave modes induced by the valve closure, different WS values can be found for the transversal and longitudinal particle motion. Furthermore, the ratio of tissue motion amplitudes in both directions can be an indicator of the wave modes induced.
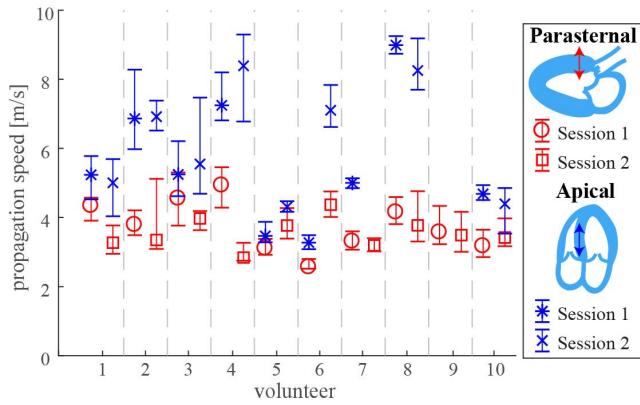
Fig. 6. Overview of the median propagation speeds and their IQR obtained in parasternal and apical view.

B. Experimental Results

Fig. 6 shows the median WS and interquartile ranges (IQR) obtained for the measurements in human in parasternal and apical views. The median WS varied between 3.2 and 4.3 m/s for parasternal view, and 3.5 and 8.7 m/s for apical view. It should be noted again that the number of measurements performed in the two views differed. Furthermore, the number of heart cycles captured in a single recording varied depending on the heart rate of the volunteer. Moreover, recordings with the poor B-mode quality or with no visible propagating waves were excluded (13% of acquisitions). This resulted in a different total number of WS estimations for both views: $n = 490$ for apical and $n = 970$ for parasternal view. Propagation speeds above 10 m/s were assumed to be nonphysical and were, therefore, excluded (apical exclusion: 14%, 68/490; parasternal exclusion: 0%, 0/970). For volunteer 9, no visible propagating wave with a speed below 10 m/s was measured in an apical view.

An overview of the statistical results is shown in Table II. As a first major result, for all sessions and all volunteers, we obtained higher median WS in apical than in the parasternal view. A mean difference of -2.0 m/s was found (Bland–Altman analysis, LOA: -5.3–1.4 m/s, range: -4.7–0.76 m/s) [see Fig. 7(a)]. The differences were found to be statistically significant (Wilcoxon signed-rank test, $n = 9$, $p < 0.01$). We found a median for the median WS per volunteer per session of 3.8 m/s ($n = 10$, range: 3.2–4.3 m/s) and 5.1 m/s ($n = 9$, range: 3.5–8.7 m/s) in parasternal and apical view, respectively.

As a second major result, no correlation was found between the WS in the two views ($r = 0.26$, $p = 0.49$) [see Fig. 7(b)]. Moreover, Fig. 7(a) shows that the difference in WS in general increases with the mean WS of the parasternal and apical view. Such a trend in a Bland–Altman plot indicates again that the two measured variables have low correlation, as was seen with the correlation test, and/or that either has a high variance. To further investigate the differences in WS among the two views, the difference correlated with the WS in apical view ($r = -0.98$, $p < 0.01$) and not to the WS in parasternal view ($r = -0.056$, $p = 0.89$). When combining these statistical observations, we conclude that the differences between the

two views are mainly caused by the intervolunteer variance of the apical view measurements, and not of the parasternal view measurements.

As described in Section II, five instead of one apical view measurements were recorded for volunteers 1–4 in the second scanning session. Fig. 6 shows that the results obtained in the second session in the apical view for these volunteers are within the IQR of the corresponding results in the first session. This suggests that the interscan variability in apical view is small compared with the intrascan variability.

Test–retest variability was tested by comparing the median values per volunteer per session. No statistically significant differences were found in the apical view (Wilcoxon signed-rank test, $n = 8$, $p = 0.31$) and parasternal view (Wilcoxon signed-rank test, $n = 10$, $p = 0.43$) between the sessions. The mean differences were found to be -0.61 m/s (Bland-Altman analysis, LOA: -3.4–2.2 m/s, range: -3.8–0.74 m/s) and 0.20 m/s (Bland–Altman analysis, LOA: -1.8–2.2 m/s, range: -1.8–2.1 m/s) for the apical and parasternal view, respectively.

Although the parasternal and apical views were chosen to approximate a, respectively, horizontal and vertical orientation of the IVS, variations in IVS angular orientation still occurred between acquisitions. This angular orientation was taken into account by manually drawing M-lines that are aligned with the orientation of the IVS. This way, the wave propagation was measured along the global orientation of the IVS. However, since the one-lag autocorrelation method is sensitive to axial tissue motion only, the tracking in the respective views could neither be attributed to purely longitudinal nor purely transversal particle motion in the IVS. By measuring the absolute angle $|\theta|$ between the M-line and ultrasound beam direction at the center of the M-line, the effect of M-line orientation with respect to the probe was tested in Fig. 8. For the parasternal view measurements, a weak correlation between the WS and angle was found ($r = 0.34$, $p < 0.01$). The WS values were found to increase with the increasing angle between M-line and axial directions. For the apical view measurements, no significant correlation was found ($r = -0.06$, $p = 0.2$). Although this could be partly explained by the limited number of WS values obtained in apical view, also no trend in WS with respect to $|\theta|$ is visible in Fig. 8(b).

IV. Discussion

A. General Findings

The propagation speeds of the natural mechanical waves induced after AVC measured in apical and parasternal view in ten healthy volunteers were compared in this study. This study has three main findings. First, the WS measured in apical view was found to be statistically higher than in parasternal view (median (IQR) of 5.1 m/s (4.5–7.2 m/s) versus 3.8 m/s (3.4–4.0 m/s), $p < 0.01$, $n = 9$). Although these values are in the same range as the literature values (mean $\pm$ standard deviation, parasternal: 3.7 ± 0.4 m/s, apical: 5.7 ± 1.8 m/s, see Table I), they contradict the statement by Kanai [19] that the propagation speeds measured in parasternal and apical view are similar. Second, no correlation was found between

TABLE II
OVERVIEW OF THE STATISTICAL CHARACTERISTICS OF THIS STUDY. VALUES DENOTED WITH AN ASTERISK(∗) ARE STATISTICALLY SIGNIFICANT
($p < 0.05$). ABBREVIATIONS: LOA: LIMITS OF AGREEMENT BLAND-ALTMAN ANALYSIS (± 1.96 SD) AND IVS: INTERVENTRICULAR SEPTUM

|	Performed test	Statistics	
Apical vs Parasternal	Wilcoxon signed-rank test on median propagation speeds per volunteer measured in apical vs parasternal view	p=0.0078*, n=9	
	Bland-Altman: medians of parasternal – apical view per volunteer	Mean: -2.0 m/s LOA: -5.3 - 1.4 m/s Range: -4.7 - 0.76 m/s	
	Linear correlation of medians in apical and parasternal view	r=0.26, p=0.49	
	Linear correlation of differences in medians of the 2 views with the median in parasternal view	r=-0.056, p=0.89	
	Linear correlation of differences in medians of the 2 views with the median in apical view	r=-0.98*, p<0.01	
		Apical View	**Parasternal View**
Inter-volunteer variability	Median of median propagation speeds per volunteer	Median: 5.1 m/s, n=9 IQR: 4.5 - 7.2 m/s Range: 3.5 - 8.7 m/s	Median: 3.8 m/s, n=10 IQR: 3.4 - 4.0 m/s Range: 3.2 - 4.3 m/s
Test-retest variability	Wilcoxon signed-rank test on median propagation speeds per volunteer measured in session 1 and session 2	p=0.31, n=8	p=0.43, n=10
	Bland-Altman: median propagation speeds per volunteer measured in session 1 – session 2	Mean: -0.61 m/s LOA: -3.4 - 2.2 m/s Range: -3.8 - 0.74 m/s	Mean: 0.20 m/s LOA: -1.8 - 2.2 m/s Range: -1.8 - 2.1 m/s
IVS orientation	Linear correlation of angle between M-line and axial direction and propagation speed	r=-0.06, p=0.2	r=0.34*, p<0.01
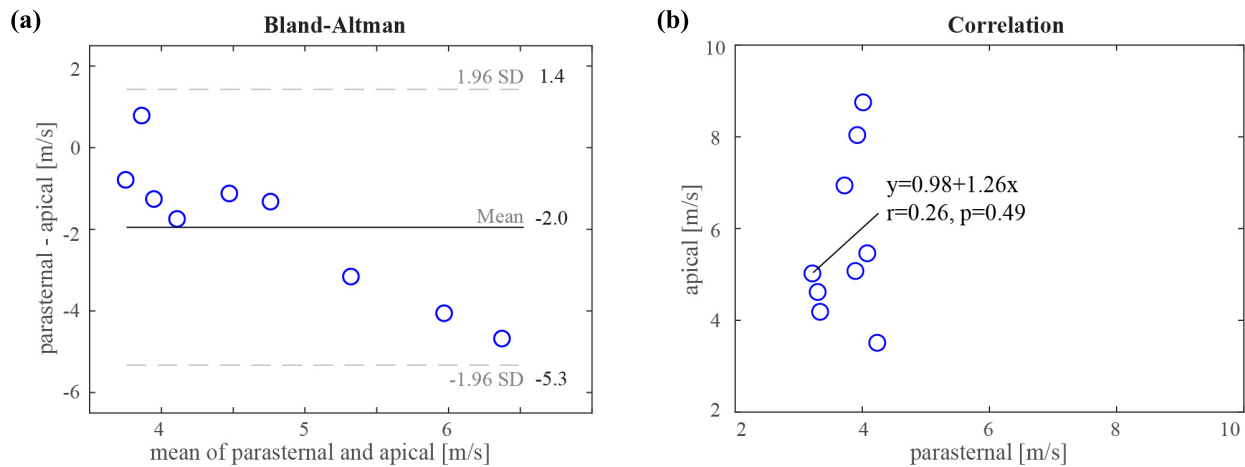
Fig. 7. (a) Bland–Altman analysis of the median propagation speeds obtained per volunteer for the velocity panels. (b) No correlation was found between the propagation speeds obtained in apical and parasternal view.

the WS measured in the two views ($r = 0.26$, $p = 0.49$). Third, an unexpectedly large intervolunteer variability among healthy volunteers was found in the apical view (3.5–8.7 m/s) versus parasternal view (3.2–4.3 m/s).

B. Relation With Lamb Waves

Our hypothesis posed in the introduction was that both A_0- and S_0-mode Lamb waves were excited, but that only one could be measured in each view. We measured statistically higher WS in apical than in the parasternal view, which would support the hypothesis. Since one wave mode cannot have different WS along the same propagation path for the same frequency components, measuring two different WS in the two views suggests that different wave modes are

measured. Furthermore, the simulations show that if one single wave mode is induced, similar WS are obtained; if different wave modes are induced simultaneously, different WS can be measured for the different particle-motion components. However, both modes would depend on the same material constants and would, thus, be related, but we did not find a linear correlation between the WS obtained in both views ($r = 0.26$, $p = 0.49$), suggesting that these measurements cannot be explained by a conventional Lamb wave model.

Since both A_0- and S_0-modes include transversal, as well as longitudinal tissue motion, also a combination of different wave modes could have been measured. To what extent the different wave modes are measured in the different views
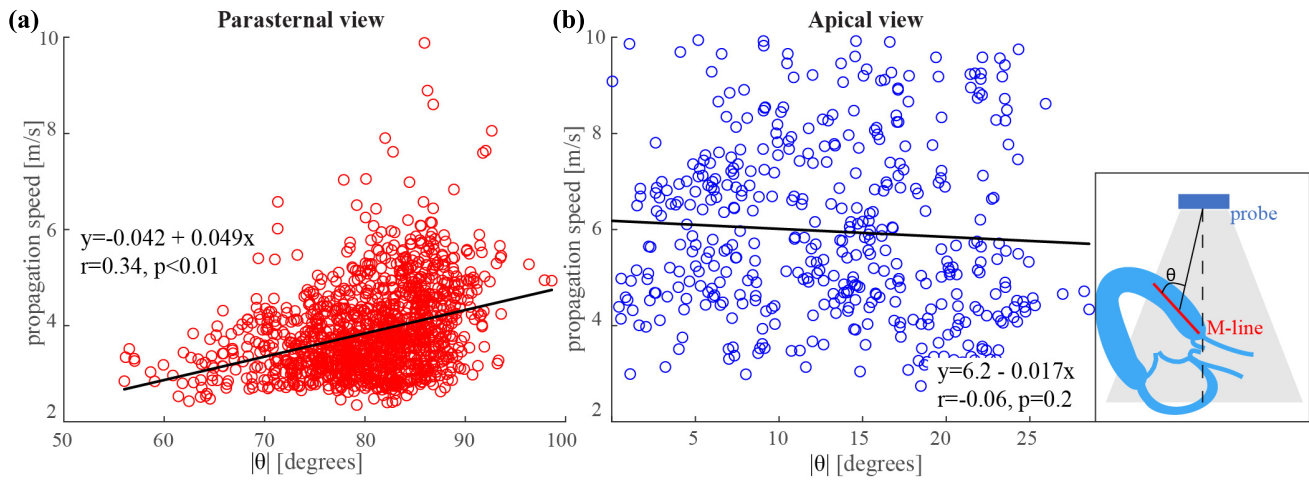
Fig. 8. (a) Weak positive correlation was found between the propagation speed values measured in parasternal view with more horizontally aligned M-lines. (b) No correlation between propagation speed values measured in apical view and this angle was found.

could depend on the exact imaging plane, image quality, volunteer, and the induced respective wave amplitudes. As an illustration, if a dominating A-wave is induced, the corresponding longitudinal tissue motion could interfere with the longitudinal tissue motion corresponding to an inferior S-wave being excited simultaneously. If the ratio of these waves differs per individual, this could have caused the variations in WS among the healthy volunteers. A smaller intervolunteer variability was found for parasternal view (3.2–4.3 m/s) than for apical view (3.5–8.7 m/s), which could suggest that the measurements in parasternal view are less affected by the interference of different wave modes, possibly due to the presence of a dominating transversal wave mode, which might loosely be called the "shear wave."

Furthermore, in additional simulations (data not shown), we found that the exact orientation of tracking direction with respect to the wave propagation direction has an effect if the amplitudes of the wave modes differ significantly. In fact, while simulating a high-amplitude A_0 and low-amplitude S_0, the tracked propagation speed of the S_0 was strongly reduced by a minor change of rotation of the tissue. Based on these simulations, one could expect lower WS in measurements with a more horizontal IVS (see Fig. 8(a); 90° indicates a horizontal M-line) if both A_0- and S_0-waves are induced. This is contradicted by our experimental results: we found a weak positive linear correlation between the WS and angle in the parasternal view and no correlation in apical view (see Fig. 8). Therefore, the results of this study do not support the above hypotheses of either single or a superposition of pure Lamb waves. For this reason, we refrain from converting WS to physical quantities of myocardial stiffness in this study.

C. Apical View Measurements

In principle, other phenomena might have caused the unexpectedly large intervolunteer variability in apical view (3.5–8.7 m/s) versus parasternal view (3.2–4.3 m/s). A possible cause is variability in image plane in the apical view. In an apical four-chamber view, the aortic valve—source of wave excitation—is not in the imaging plane and possibly, therefore, measuring waves after AVC is more challenging. This also

gives the sonographer more freedom when selecting the image plane, possibly causing extra variability. By using an apical three-chamber view, the same plane would be imaged as in a parasternal long-axis view. However, we experienced difficulties in obtaining an acoustic window with a vertically oriented IVS in an apical three-chamber view due to limited acoustic access for the first few volunteers and, therefore, decided to only record apical four-chamber views to improve feasibility and repeatability of the acoustic window among the volunteers. Furthermore, other apical studies of the natural waves after AVC in the literature also used the four-chamber view [20], [26]. The impact of the selected apical view needs further investigation, for which a larger study population is better suited to cope with a larger fraction of unmeasurable three-chamber views.

The used Lamb-wave model assumes a fluid-immersed elastic plate which might be too simplistic for the viscoelastic hyperelastic anisotropic IVS *in vivo* [44]. Furthermore, the apical view measurements track different tissue motion components with respect to fiber orientation. This suggests that apical WS measurements might provide additional information about the heart's mechanical properties, next to parasternal WS measurements. However, this statement should still be proven in future physiologic studies.

D. Study Limitations

The parasternal wave measurements were repeated five times per volunteer per session, whereas, there was only one measurement for the apical wave recordings. Despite this limited number of apical view measurements, only one volunteer showed a remarkable disagreement in apical view for the different sessions (volunteer 6 in Fig. 6), possibly due to the different location of the IVS in the FOV. The other volunteers showed a fair agreement between the apical sessions. Furthermore, for the first four volunteers, we also recorded five measurements in apical view in the second session. Compared with the intrascan variability, no large interscan variability was found, thus validating our approach to only record one single clip in apical view for most volunteers.
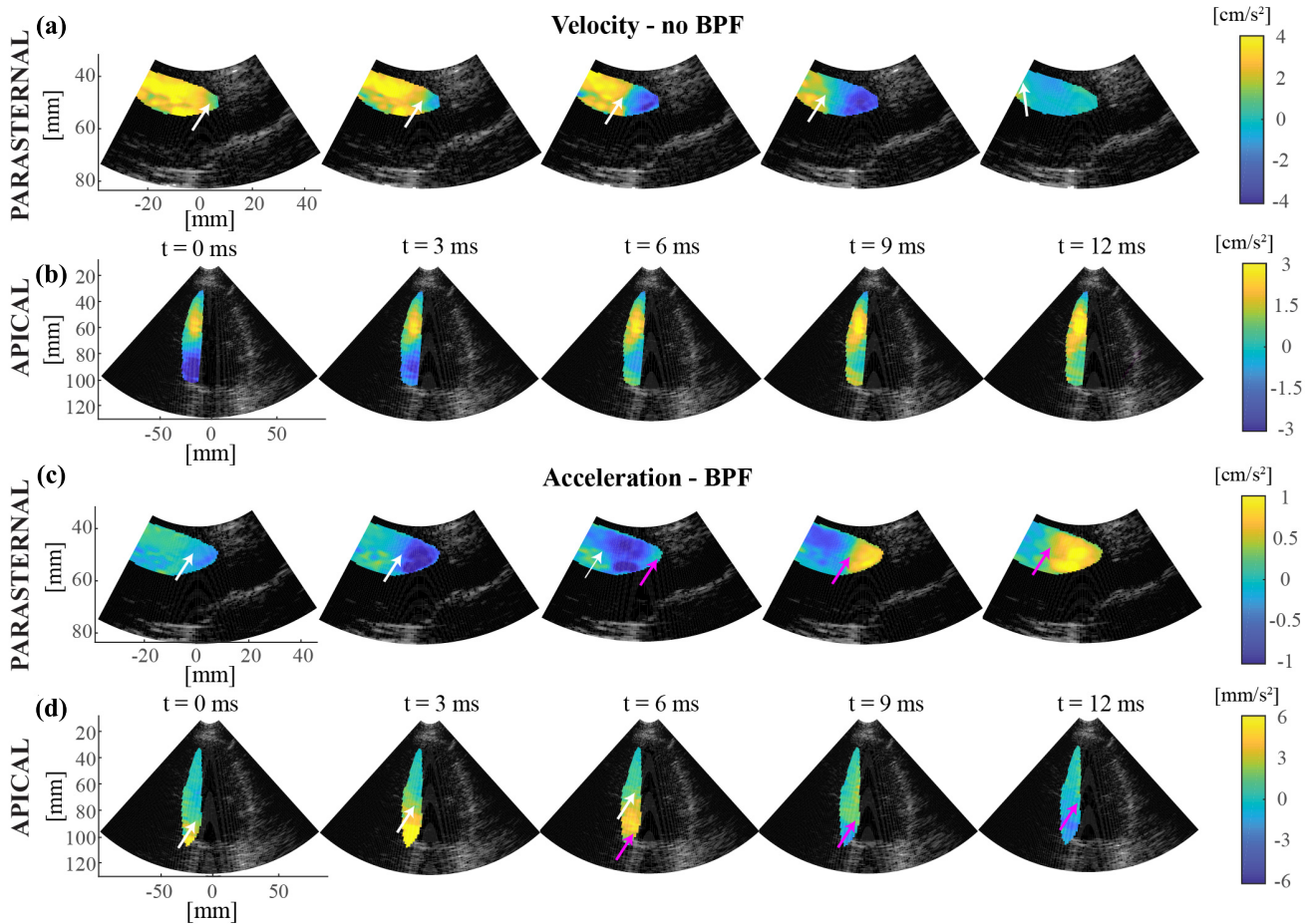
Fig. 9. Propagation of the waves after AVC in (a) and (c) parasternal and (b) and (d) apical view. (a) and (b) Velocity tissue Doppler values as well as (c) and (d) acceleration tissue Doppler values after applying a bandpass filter are shown in the figure. White and pink arrows depict the propagation of the waves. No clear propagating wave is seen in the apical view when using the tissue velocity values, in contrast to when using acceleration values.

These observations show that the measurements in the apical view are at least repeatable.

References [6], [7], and [30] also report the use of tissue acceleration panels instead of tissue velocity panels, which allows an easier detection of a "wave pattern" propagating over the IVS (see lower two rows of Fig. 9) as slower motion (such as cardiac rotation or translation as the heart starts to relax) is suppressed. However, when using acceleration panels in this study, different WS were obtained than when using tissue velocities, confirming observations in [27]. Additionally, we obtained more WS values above 10 m/s, which were assumed to be nonphysical (apical view: 31% versus 14%; parasternal view: 1% versus 0% excluded). Therefore, we used tissue velocities instead of tissue accelerations in this study to investigate the differences measured in parasternal and apical views.

E. Clinical Application

For the application in clinical diagnosis, significant differences between WS estimations after AVC in healthy and diseased myocardium should be measured. First clinical studies of natural mechanical waves after AVC in parasternal view obtained higher WS values for cardiac amyloidosis and hypertrophic patients [7], [8]. To the best of our knowledge, no clinical studies using WS measurements after AVC in apical view have been published yet. This study showed a lower intervolunteer variability in parasternal view (3.2–4.3 m/s in parasternal view versus 3.5–8.7 m/s in apical view), which is an advantage for a more robust clinical diagnosis. However, the cause of the observed high intervolunteer variability in apical view should still be further investigated, preferably while taking an apical four-chamber and three-chamber view into account. The 3-D acquisitions with a high temporal and spatial resolution to measure different tissue motion components and simultaneously measure the propagation direction would be beneficial for this purpose. Since higher WS corresponding to larger wavelengths for the same frequency can be tracked less accurate due to the limited IVS length and limited frame rate [27], it is an advantage for accuracy and precision to measure lower normal WS for healthy volunteers in parasternal view. Therefore, our results in combination with initial proof of clinical relevance suggest that parasternal WS measurements are currently favorable for robust clinical diagnosis. However, parasternal and apical view measurements might contain additional information about myocardial material properties, which could potentially improve current disease diagnosis. Further study should, thus, investigate the clinical added value of apical WS.

V. CONCLUSION

This study compared the propagation speeds of natural mechanical waves after AVC in apical and parasternal view in ten healthy volunteers. Significantly higher propagation speeds were obtained in apical than in parasternal view (median (IQR) of 5.1 m/s (4.5–7.2 m/s) versus 3.8 m/s (3.4–4.0 m/s), $p < 0.01$, $n = 9$). The propagation speeds in the different views were not correlated ($r = 0.26$, $p = 0.49$). Furthermore, an unexpectedly large intervolunteer variability among healthy volunteers was found in the apical view (3.5–8.7 versus 3.2–4.3 m/s in the parasternal view). According to our statistics, the theory of Lamb waves alone cannot explain the differences in propagation speeds measured in the two views. However, the parasternal long-axis view seems to be preferred in future clinical diagnosis, as this view resulted in lower intervolunteer variabilities and has been earlier shown to relate to several diseases.

ACKNOWLEDGMENT

REFERENCES

[1] P. Ponikowski *et al.*, "2016 ESC Guidelines for the diagnosis and treatment of acute and chronic heart failure," *Eur. Heart J.*, vol. 37, no. 27, pp. 2129–2200, 2016.

[2] R. M. Lang *et al.*, "Recommendations for cardiac chamber quantification by echocardiography in adults: An update from the American Society of Echocardiography and the European Association of Cardiovascular Imaging," *Eur. Hear. J.-Cardiovasc. Imag.*, vol. 16, no. 3, pp. 233–371, 2015.

[3] S. F. Nagueh *et al.*, "Recommendations for the evaluation of left ventricular diastolic function by echocardiography: An update from the American Society of Echocardiography and the European association of cardiovascular imaging," *J. Amer. Soc. Echocardiogr.*, vol. 29, no. 4, pp. 277–314, Apr. 2016.

[4] J. U. Voigt, "Direct stiffness measurements by echocardiography: Does the search for the holy grail come to an end?" *JACC Cardiovasc. Imag.*, vol. 12, no. 7, pp. 1146–1148, 2019.

[5] D. A. Kass, J. G. F. Bronzwaer, and W. J. Paulus, "What mechanisms underlie diastolic dysfunction in heart failure?" *Circulat. Res.*, vol. 94, no. 12, pp. 1533–1542, Jun. 2004.

[6] P. Santos *et al.*, "Natural shear wave imaging in the human heart: Normal values, feasibility, and reproducibility," *IEEE Trans. Ultrason., Ferroelectr., Freq. Control*, vol. 66, no. 3, pp. 442–452, Mar. 2019.

[7] A. Petrescu *et al.*, "Velocities of naturally occurring myocardial shear waves increase with age and in cardiac amyloidosis," *JACC, Cardiovascular Imag.*, vol. 12, no. 12, pp. 2389–2398, Dec. 2019.

[8] M. Strachinaru *et al.*, "Naturally occurring shear waves in healthy volunteers and hypertrophic cardiomyopathy patients," *Ultrasound Med. Biol.*, vol. 45, no. 8, pp. 1977–1986, Aug. 2019.

[9] O. Villemain *et al.*, "Myocardial stiffness evaluation using noninvasive shear wave imaging in healthy and hypertrophic cardiomyopathic adults," *JACC, Cardiovascular Imag.*, vol. 12, no. 7, pp. 1135–1145, Jul. 2019.

[10] M. W. Urban, C. Pislaru, I. Z. Nenadic, R. R. Kinnick, and J. F. Greenleaf, "Measurement of viscoelastic properties of *in vivo* swine myocardium using Lamb wave dispersion ultrasound vibrometry (LDUV)," *IEEE Trans. Med. Imag.*, vol. 32, no. 2, pp. 247–261, Feb. 2013.

[11] C. Pislaru, M. W. Urban, S. V. Pislaru, R. R. Kinnick, and J. F. Greenleaf, "Viscoelastic properties of normal and infarcted myocardium measured by a multifrequency shear wave method: Comparison with pressure-segment length method," *Ultrasound Med. Biol.*, vol. 40, no. 8, pp. 1785–1795, Aug. 2014.

[12] H. Tzschätzsch *et al.*, "*in vivo* time harmonic elastography of the human heart," *Ultrasound Med. Biol.*, vol. 38, no. 2, pp. 214–222, Feb. 2012.

[13] R. R. Bouchard, S. J. Hsu, P. D. Wolf, and G. E. Trahey, "*in vivo* cardiac, acoustic-radiation-force-driven, shear wave velocimetry," *Ultrason. Imag.*, vol. 31, no. 3, pp. 201–213, Jul. 2009.

[14] M. Couade *et al.*, "*in vivo* quantitative mapping of myocardial stiffening and transmural anisotropy during the cardiac cycle," *IEEE Trans. Med. Imag.*, vol. 30, no. 2, pp. 295–305, Feb. 2011.

[15] P. J. Hollender, P. D. Wolf, R. Goswami, and G. E. Trahey, "Intracardiac echocardiography measurement of dynamic myocardial stiffness with shear wave velocimetry," *Ultrasound Med. Biol.*, vol. 38, no. 7, pp. 1271–1283, Jul. 2012.

[16] M. Pernot *et al.*, "Shear wave imaging of passive diastolic myocardial stiffness: Stunned versus infarcted myocardium," *JACC, Cardiovasc. Imag.*, vol. 9, no. 9, pp. 1023–1030, 2016.

[17] M. Pernot, M. Couade, P. Mateo, B. Crozatier, R. Fischmeister, and M. Tanter, "Real-time assessment of myocardial contractility using shear wave imaging," *J. Amer. College Cardiol.*, vol. 58, no. 1, pp. 65–72, Jun. 2011.

[18] P. Song *et al.*, "Quantitative assessment of left ventricular diastolic stiffness using cardiac shear wave elastography: A pilot study," *J. Ultrasound Med.*, vol. 35, no. 7, pp. 1419–1427, May 2016.

[19] H. Kanai, "Propagation of spontaneously actuated pulsive vibration in human heart wall and *in vivo* viscoelasticity estimation," *IEEE Trans. Ultrason., Ferroelect., Freq. Control*, vol. 52, no. 11, pp. 1931–1942, Nov. 2005.

[20] B. Brekke *et al.*, "Ultra-high frame rate tissue Doppler imaging," *Ultrasound Med. Biol.*, vol. 40, no. 1, pp. 222–231, Jan. 2014.

[21] H. J. Vos *et al.*, "Cardiac shear wave velocity detection in the porcine heart," *Ultrasound Med. Biol.*, vol. 43, no. 4, pp. 753–764, Apr. 2017.

[22] M. Pernot, K. Fujikura, S. D. Fung-Kee-Fung, and E. E. Konofagou, "ECG-gated, mechanical and electromechanical wave imaging of cardiovascular tissues *in vivo*," *Ultrasound Med. Biol.*, vol. 33, no. 7, pp. 1075–1085, Jul. 2007.

[23] C. Pislaru, M. M. Alashry, J. J. Thaden, P. A. Pellikka, M. Enriquez-Sarano, and S. V. Pislaru, "Intrinsic wave propagation of myocardial stretch, a new tool to evaluate myocardial stiffness: A pilot study in patients with aortic stenosis and mitral regurgitation," *J. Amer. Soc. Echocardiogr.*, vol. 30, no. 11, pp. 1070–1080, Nov. 2017.

[24] M. Strachinaru *et al.*, "Myocardial stretch post-atrial contraction in healthy volunteers and hypertrophic cardiomyopathy patients," *Ultrasound Med. Biol.*, vol. 45, no. 8, pp. 1987–1998, Aug. 2019.

[25] C. Pislaru, P. A. Pellikka, and S. V. Pislaru, "Wave propagation of myocardial stretch: Correlation with myocardial stiffness," *Basic Res. Cardiol.*, vol. 109, no. 6, Sep. 2014.

[26] S. Salles, L. Løvstakken, S. A. Aase, T. G. Bjåstad, and H. Torp, "Clutter filter wave imaging," *IEEE Trans. Ultrason., Ferroelectr., Freq. Control*, vol. 66, no. 9, pp. 1444–1452, Sep. 2019.

[27] M. Strachinaru *et al.*, "Cardiac shear wave elastography using a clinical ultrasound system," *Ultrasound Med. Biol.*, vol. 43, no. 8, pp. 1596–1606, Aug. 2017.

[28] L. B. H. Keijzer *et al.*, "Reproducibility of natural shear wave elastography measurements," *Ultrasound Med. Biol.*, vol. 45, no. 12, pp. 3172–3185, Dec. 2019.

[29] P. Santos, L. Løvstakken, E. Samset, and J. D'Hooge, "Volumetric imaging of fast mechanical waves in the heart using a clinical ultrasound system: A feasibility study," in *Proc. IEEE Int. Ultrason. Symp. (IUS)*, Sep. 2017, pp. 1–5.

[30] L. Keijzer, J. G. Bosch, M. D. Verweij, N. de Jong, and H. J. Vos, "Intra-scan variability of natural shear wave measurements," in *Proc. IEEE Int. Ultrason. Symp. (IUS)*, Oct. 2018, pp. 1–4.

[31] J. Brum, "Transverse wave propagation in bounded media," in *Ultrasound Elastography for Biomedical Applications and Medicine*. Hoboken, NJ, USA: Wiley, 2019, pp. 90–104.

[32] G.-Y. Li *et al.*, "Guided waves in pre-stressed hyperelastic plates and tubes: Application to the ultrasound elastography of thin-walled soft materials," *J. Mech. Phys. Solids*, vol. 102, pp. 67–79, May 2017.

[33] I. Z. Nenadic, M. W. Urban, C. Pislaru, D. Escobar, L. Vasconcelos, and J. F. Greenleaf, "*in vivo* open- and closed-chest measurements of left-ventricular myocardial viscoelasticity using Lamb wave dispersion ultrasound vibrometry (LDUV): A feasibility study," *Biomed. Phys. Eng. Express*, vol. 4, no. 4, Apr. 2018, Art. no. 047001.

[34] I. Z. Nenadic, M. W. Urban, S. Aristizabal, S. A. Mitchell, T. C. Humphrey, and J. F. Greenleaf, "On Lamb and Rayleigh wave convergence in viscoelastic tissues," *Phys. Med. Biol.*, vol. 56, no. 20, pp. 6723–6738, Oct. 2011.

[35] I. Z. Nenadic, M. W. Urban, M. Bernal, and J. F. Greenleaf, "Phase velocities and attenuations of shear, Lamb, and Rayleigh waves in plate-like tissues submerged in a fluid (L)," *J. Acoust. Soc. Amer.*, vol. 130, no. 6, pp. 3549–3552, Dec. 2011.

[36] J. L. Rose, "Waves in plates," in *Ultrasonic Waves in Solid Media*. Cambridge, U.K.: Cambridge Univ. Press, 1999, pp. 101–132.

[37] A. Caenen *et al.*, "Effect of ultrafast imaging on shear wave visualization and characterization: An experimental and computational study in a pediatric ventricular model," *Appl. Sci.*, vol. 7, no. 8, p. 840, Aug. 2017.

[38] W.-N. Lee *et al.*, "Mapping myocardial fiber orientation using echocardiography-based shear wave imaging," *IEEE Trans. Med. Imag.*, vol. 31, no. 3, pp. 554–562, Mar. 2012.

[39] M. Wang, B. Byram, M. Palmeri, N. Rouze, and K. Nightingale, "Imaging transverse isotropic properties of muscle by monitoring acoustic radiation force induced shear waves using a 2-D matrix ultrasound array," *IEEE Trans. Med. Imag.*, vol. 32, no. 9, pp. 1671–1684, Sep. 2013.

[40] A. Caenen, M. Pernot, M. Peirlinck, L. Mertens, A. Swillens, and P. Segers, "An in silico framework to analyze the anisotropic shear wave mechanics in cardiac shear wave elastography," *Phys. Med. Biol.*, vol. 63, no. 7, Mar. 2018, Art. no. 075005.

[41] M. W. Urban, B. Qiang, P. Song, I. Z. Nenadic, S. Chen, and J. F. Greenleaf, "Investigation of the effects of myocardial anisotropy for shear wave elastography using impulsive force and harmonic vibration," *Phys. Med. Biol.*, vol. 61, no. 1, pp. 365–382, 2016.

[42] I. Pelivanov *et al.*, "Does group velocity always reflect elastic modulus in shear wave elastography?" *J. Biomed. Opt.*, vol. 24, no. 7, Jul. 2019, Art. no. 076003.

[43] M. L. Palmeri, B. Qiang, S. Chen, and M. W. Urban, "Guidelines for finite-element modeling of acoustic radiation force-induced shear wave propagation in tissue-mimicking media," *IEEE Trans. Ultrason., Ferroelectr., Freq. Control*, vol. 64, no. 1, pp. 78–92, Jan. 2017.

[44] N. C. Rouze, M. H. Wang, M. L. Palmeri, and K. R. Nightingale, "Finite element modeling of impulsive excitation and shear wave propagation in an incompressible, transversely isotropic medium," *J. Biomech.*, vol. 46, no. 16, pp. 2761–2768, Nov. 2013.

Daniel J. Bowen received the B.Sc. degree in clinical physiology from Middlesex University, London, U.K., in 2013.

He was a Cardiac Physiologist with Colchester General Hospital, Colchester, U.K., from 2010 to 2014. He trained in echocardiography at Papworth Hospital, Cambridge, U.K., from 2014 to 2017. He has been a Research Echocardiographer with the Department of Cardiology, Erasmus Medical Center (MC), Rotterdam, The Netherlands, since 2018, where he collaborates with the Department of Biomedical Engineering to aid the research and development of novel ultrasound modalities. He holds European Association of Cardiovascular Imaging (EACVI) accreditation in adult echocardiography. His research interests include detailed 2-D/3-D echo assessment in advanced heart failure and cardiomyopathies.

Annette Caenen (Member, IEEE) was born in Genk, Belgium, in September 1988. She received the M.S. degree in civil engineering from the Catholic University of Leuven, Leuven, Belgium, in 2011, and the M.S. and Ph.D. degrees in biomedical engineering from Ghent University, Ghent, Belgium, in 2013 and 2018, respectively.

She was a Visiting Scholar with Physics for Medicine Paris, Paris, France, and Duke University, Durham, NC, USA. She currently works as an FWO Postdoctoral Fellow with the IBiTech-bioMMeda Lab, Ghent University, Ghent, Belgium, the Cardiovascular Imaging and Dynamics Laboratory, Catholic University of Leuven, Leuven, Belgium, and the Department of Biomedical Engineering, Thorax Center, Erasmus Medical Center (MC), Rotterdam, The Netherlands. Her research interests are shear wave elastography, biomechanics, finite-element modeling, and noninvasive material characterization, with a focus on cardiac applications.

Lana B. H. Keijzer (Student Member, IEEE) received the B.Sc. and M.Sc. degrees in applied physics with a specialization in medical and acoustical waveform imaging from the Delft University of Technology, Delft, The Netherlands, in 2013 and 2015, respectively, and the M.Sc. degree in management of technology from the Delft University of Technology, Delft, The Netherlands, in 2016. She is currently pursuing the Ph.D. degree with the Department of Biomedical Engineering, Thorax Center, Erasmus Medical Center, Rotterdam, The Netherlands. Her Ph.D. thesis focuses on cardiac shear wave elastography measurements.

Mihai Strachinaru received the M.D. degree and the master's degree in cardiology from the Carol Davila University of Medicine and Pharmacy, Bucharest, Romania, in 2001 and 2008, respectively, and the Ph.D. degree in shear wave echocardiography from the Department of Biomedical Engineering, Erasmus Medical Center (MC), Rotterdam, The Netherlands, in 2020.

He worked as a Cardiologist at the Centre Hospitalier de Charleville-Mézières, Charleville-Mézières, France, from 2008 to 2009, Brugmann University Hospital, Brussels, Belgium, from 2009 to 2016, and Erasmus Medical Center, Rotterdam, The Netherlands, from 2016 to 2019. During this period, he developed a keen interest in cardiac noninvasive imaging, especially echocardiography. He currently holds Romanian, French, and European certifications in transthoracic and transesophageal echocardiography. He is currently a Post-Doctoral Researcher with Erasmus MC, and an Intensive Care Cardiologist with the CHIREC Hospital, Brussels, Belgium. He also works as an Imaging Consultant with Cardialysis Echocardiography Core Laboratory, Rotterdam. His research interests include high-frame-rate imaging in all its aspects: 2-D and 3-D, cardiac shear waves, ultrafast Doppler, contrast imaging, and related preclinical and clinical applications.

Antonius F. W. van der Steen (Fellow, IEEE) received the M.Sc. degree in applied physics from Technical University, Delft, The Netherlands, in 1989, and the Ph.D. degree in medical sciences from the Radboud University of Nijmegen, Nijmegen, The Netherlands, in 1994.

He is currently the Head of biomedical engineering with Thorax Center, Erasmus Medical Center (MC), Rotterdam, The Netherlands. He is the Co-Founder and the current Chairman of the Board of the Medical Delta, a collaboration between Erasmus MC, TU Delft, Delft, and Leiden University Medical Centre, Leiden, The Netherlands. He is currently a Professor of biomedical engineering with Erasmus MC, a Professor of applied physics with TU Delft, and an Honorary Visiting Professor with the Shenzhen Institutes of Advanced Technologies, Chinese Academy of Sciences, Shenzhen, China. His main scientific interest is in creating imaging modalities for the cardiovascular system. His main policy interest is generating technical solutions for sustainable health care.

Dr. van der Steen is the 2000 NWO PIONIER Technical Sciences and the 2007 Simon Stevin Master. He is a member of both the Netherlands Academy of Technology and Innovation and the Royal Academy of Arts and Sciences. He is a fellow of the European Society of Cardiology.

Martin D. Verweij (Member, IEEE) received the M.Sc. (*cum laude*) and Ph.D. degrees in electrical engineering from the Delft University of Technology, Delft, The Netherlands, in 1988 and 1992, respectively.

From 1993 to 1997, he was a Research Fellow with the prestigious Royal Netherlands Academy of Arts and Sciences, Amsterdam, The Netherlands. In 1995 and 1997, he was a Visiting Scientist with Schlumberger Cambridge Research, Cambridge, U.K. In 1998, he became an Assistant Professor and later that year an Associate Professor with the Laboratory of Electromagnetic Research, Delft University of Technology, where he switched to the Laboratory of Acoustical Wavefield Imaging in 2011. Since 2015, he has also a part-time position with Biomedical Engineering Group, Erasmus Medical Center, Rotterdam, The Netherlands. His research interests include dedicated transducer design, beamforming algorithms, the mathematical modeling and numerical simulation of medical ultrasound, and the physics of medical ultrasound. He is the Originator of the Iterative Nonlinear Contrast Source (INCS) method for the computation of nonlinear ultrasound fields. He is a Research Leader of the Dutch Technology Foundation (TTW-NWO) on projects involving transducer design, beamforming, and imaging.

Dr. Verweij is a fellow of the Acoustical Society of America, an Associate Editor of the *Journal of the Acoustical Society of America*, and a Treasurer of the Dutch Society for Medical Ultrasound.

Nico de Jong (Associate Member, IEEE) received the M.Sc. degree in applied physics in the field of pattern recognition from the Delft University of Technology, Delft, The Netherlands, in 1978, and the Ph.D. degree in acoustic properties of ultrasound contrast agents from the Erasmus Medical Center, Rotterdam, The Netherlands, in 1993.

Since 1980, he has been a Staff Member of biomedical engineering with Thorax Center, Erasmus University Medical Center (MC), Rotterdam, The Netherlands. From 2003 to 2011, he was a part-time Full Professor with the Physics of Fluids Group headed by Prof. D. Lohse, University of Twente, Enschede, The Netherlands. From 2011 to 2015, he was a part-time Full Professor with Technical University, Delft. In 2015, he became the Head of the Medical Imaging Group, Technical University. He teaches on Technical Universities and Erasmus MC. He has graduated 35 Ph.D. students and is currently supervising more than 10 Ph.D. students.

Dr. de Jong is the Founder and the Organizer of the Annual European Symposia (January 2020) for the 25th time on ultrasound contrast imaging, held in Rotterdam and attended by approximately 175 scientists from universities and industries all over the world. He is on the Safety Committee of World Federation of Ultrasound in Medicine and Biology (WFUMB), an Associate Editor of *Ultrasound in Medicine and Biology*, and has been a Guest Editor for special issues of several journals.

Johan G. Bosch (Member, IEEE) received the M.Sc. degree in electrical engineering from the Eindhoven University of Technology, Eindhoven, The Netherlands, in 1985, and the Ph.D. degree from the Leiden University Medical Center, Leiden, The Netherlands, in 2006.

He performed ultrasound and image processing research at Erasmus University, Rotterdam, The Netherlands, and Leiden University, Leiden. From 1995 to 2005, he was an Assistant Professor and the Head of the Echocardiography Section, Division of Image Processing (LKEB), Department of Radiology, Leiden University Medical Center. He is currently an Associate Professor and a Staff Member with the Department of Biomedical Engineering, Thorax Center, Erasmus Medical Center (MC), Rotterdam, The Netherlands. He is currently a (Co)-Leader of several projects in advanced ultrasound technology, e.g., on 3-D transducer development, 2-D and 3-D carotid and transesophageal echocardiography imaging, and ultrasound intervention guidance and monitoring. His research interests include 2-D and 3-D echographic image generation and processing/analyses, flow analysis, transducer development, and optimal border detection approaches with geometrical and statistical models.

Hendrik J. Vos (Member, IEEE) received the M.Sc. degree in applied physics from the Delft University of Technology, Delft, The Netherlands, in 2004, and the Ph.D. degree from the Department of Biomedical Engineering, Erasmus Medical Center (MC), Rotterdam, The Netherlands, in 2010.

He worked as a Postmaster Researcher with the University of Florence, Florence, Italy, and a Contract Researcher for the petrochemical industry on cutting-edge ultrasonic solutions. He is currently an Assistant Professor with Erasmus MC, and received a Dutch NWO-TTW-VIDI Personal Grant in 2018. His research interests include acoustical array technology for biomedical imaging in all its aspects: transducers, 2-D and 3-D beamforming, cardiac shear waves, ultrafast Doppler, contrast imaging, and related subclinical and clinical studies.